Comparison of Linear and Circular Polarization for Magnetic Resonance Imaging

G. H. GLOVER,* C. E. HAYES,* N. J. PELC,* W. A. EDELSTEIN,†
O. M. MUELLER,† H. R. HART,† C. J. HARDY,†
M. O'DONNELL,† AND W. D. BARBER†

*General Electric Medical Systems Group, Applied Science Laboratory, Milwaukee, Wisconsin 53201,
and †General Electric Corporate Research & Development, Schenectady, New York 12345

A comparison of experimental imaging results obtained with linearly polarized and circularly polarized radiofrequency excitation and reception is presented. Simulation images in good agreement with the experimental scans are described. The simulations are calculated with a model in which a homogeneous, isotropic cylinder of lossy dielectric material and infinite axial extent is immersed in a uniform rf magnetic field perpendicular to the axis. It is found that with the usual linear polarization, reconstructions of uniform objects have regions of decreased intensity. These artifacts are shown to arise from dielectric standing wave effects and eddy currents. The effects become more severe as the frequency or object size is increased, and depend upon the complex conductivity of the object. Results indicate that a significant reduction in the artifact intensity is achieved when circular polarization is employed for both transmission and reception. The expected benefits of circular polarization over linear polarization in reduction of excitation power (up to 50% reduction) and signal-to-noise advantage ($\sqrt{2}$) have been realized in practice with cylindrical objects and human subjects. © 1985 Academic Press, Inc.

INTRODUCTION

It is generally recognized that the signal-to-noise ratio (SNR) and contrast-to-noise ratio in magnetic resonance imaging of human subjects improve as the field strength is increased (*1–3*). This fact, when coupled with possibilities for spectroscopic applications, has stimulated interest in proton imaging at NMR frequencies in the tens of megahertz range.

The advantages of higher field are accompanied, however, by a number of engineering difficulties. One problem is the necessity for improved fractional magnet homogeneity as the field is increased. Other difficulties derive from the complexity of rf coil design and increased rf drive requirements. These problems can be overcome by suitable engineering attention using known technology.

There is, however, a concern with high-field imaging which derives from the fundamental physics of the interaction of electromagnetic energy with lossy dielectrics, which does not yield to improved engineering. This is the problem which has been referred to in the past as the "rf penetration effect" (*4*). Earlier theoretical calculations, in fact, predicted that imaging of whole-body sections would be impossible beyond about 10 MHz due to the (supposed) inability to excite an rf magnetic field within the

255

lossy body interior (5). These predictions have now clearly been shown to be too harsh by the successful use of MRI medical equipment at 0.5 T and above.

Nevertheless, artifacts have been observed in high-field whole-body imaging which can be attributed to rf effects. An example is given in Fig. 1A, which shows an image of an abdominal section produced at 63.8 MHz (1.5 T) using a single-port coil. The display window has been chosen to enhance the effects, which are manifested as areas of decreased image intensity that cannot be attributed to anatomical features. Another example is shown in Fig. 1B, wherein a water phantom (which should, of course, ideally reconstruct with uniform intensity) shows four "holes" in the image. Preliminary experiments in which the shape and conductivity of the phantom were changed indicated that the artifacts indeed resulted from rf effects.

Further experiments and simulations showed that the "quadrupole" artifact was caused by the use of linear polarization of the rf coil. It was found that circularly polarized excitation and reception substantially altered the artifact pattern and reduced the intensity of the artifacts.

It is therefore of some interest to examine how different rf field polarizations affect the MR imaging process. In the next section we present a simple model for calculation of these effects, while following sections provide experimental evidence which supports the preliminary conclusions above.
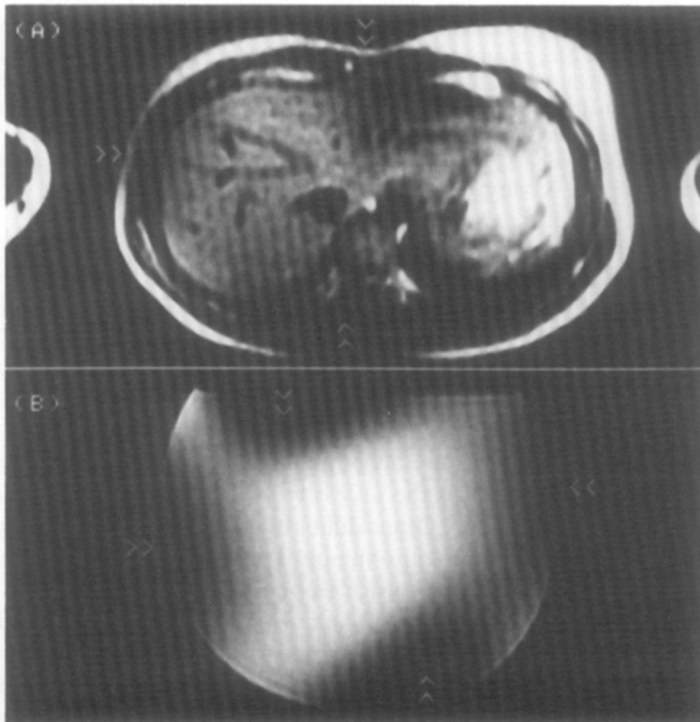

FIG. 1. Human (A) and water phantom (B) scans showing rf inhomogeneity artifacts (arrows).

SIMULATIONS OF RADIOFREQUENCY EFFECTS

Theoretical Model

A detailed model of the dielectric structure with human anatomy would prove difficult to solve, and its complexity might well detract from the intended conceptual description of the effects. We shall see, however, that a simple cylindrical model gives an adequate description of polarization effects in humans as well as in phantoms. We consider, therefore, the model shown in Fig. 2 wherein a homogeneous, lossy dielectric cylinder with infinite axial extent is embedded in an (otherwise) uniform rf magnetic field perpendicular to the axis. We wish to calculate the expected image intensity for this cylindrical object as various parameters (geometry, frequency, and dielectric characteristics) are varied.

There are three components of such a calculation of image intensity. The first is to determine the rf magnetic field distribution set up within the cylinder by the externally uniform field. This is the only component which was considered by previous authors (4, 6). The second factor is to calculate the NMR response to this excitation for a given pulse sequence. The third factor is to determine the signal intensity induced in the receiving coil from within the cylinder by the excited nuclei. The first and third factors are very similar and are addressed with a solution given originally by Mansfield and Morris (6). Their results will be generalized to include excitation having circular as well as linear polarization. A similar model was considered previously by Bottomley and Andrew (4), except that in their case the applied field direction was chosen parallel to the axis.

Radiofrequency field distribution. Consider the geometry of Fig. 2. The applied rf field, $\mathbf{B}_1$, is taken to be perpendicular to the z axis. The cylinder is assumed to comprise an isotropic, homogeneous, lossy dielectric with relative permittivity ϵ_r and conductivity σ, or resistivity $\rho = \sigma^{-1}$.
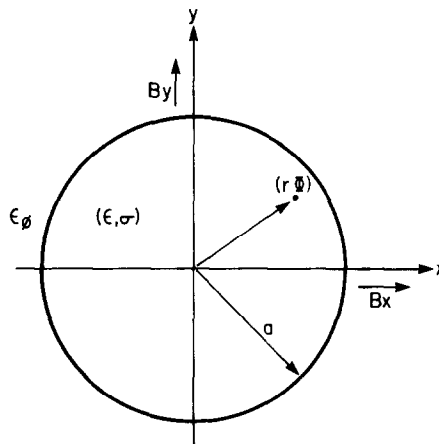

FIG. 2. Cylindrical geometry for simulations. Object is homogeneous and is infinite in z direction. Linearly polarized excitation components are shown.

This problem was solved (6) for linear polarization of the rf field with $\mathbf{B}_1 = B_{1x}\mathbf{a}_x$, where $\mathbf{a}_x$ is a unit vector in the x direction. The transverse field components for such excitation were shown to be

$$\mathbf{B}_{tx}(r, \phi) = (b_{xx}\mathbf{a}_x + b_{yx}\mathbf{a}_y)B_{1x},$$ [1]

where

$$b_{xx} = \psi_1 \cos 2\phi + \psi_0,$$

$$b_{yx} = \psi_1 \sin 2\phi,$$ [2]

$$\psi_1 = \frac{1}{J_0(ka)}\left[\frac{2J_1(kr)}{kr} - J_0(kr)\right]$$ [3]

$$\psi_0 = \frac{J_0(kr)}{J_0(ka)},$$ [4]

$J_0(x)$ and $J_1(x)$ are Bessel functions of the first kind, $\mathbf{a}_y$ is a unit vector in the y direction, and k is a complex wavenumber given by

$$k = 2\pi/\lambda,$$ [5]

where

$$\lambda = \lambda_0/\sqrt{\epsilon_r - i/\omega\epsilon_0\rho},$$ [6]

and

$$\lambda_0 = 2\pi/\omega\sqrt{\mu_0\epsilon_0}.$$ [7]

In these equations, λ_0 is the free space wavelength given in terms of the permittivity and permeability of free space, ϵ_0 and μ_0, respectively, λ is the reduced wavelength within the cylinder, $i = \sqrt{-1}$, and (r, ϕ) denote cylindrical coordinates. A factor of $e^{i\omega t}$ is understood for the field components.

We may represent $\mathbf{B}_t$ in terms of rotating components by noting that any sinusoidally varying vector field $\mathbf{B} = b_x\mathbf{a}_x + b_y\mathbf{a}_y$ can be expressed in terms of rotating components as $\mathbf{B} = (b_x + ib_y)\mathbf{a}^+ + (b_x^* + ib_y^*)\mathbf{a}^-$, where $\mathbf{a}^\pm$ represent vectors rotating at an angular frequency ω in the clockwise ($-$) or counterclockwise ($+$) direction (9) and $*$ denotes a complex conjugate. We suppose that the main NMR polarizing field direction has been chosen such that the $+$rf rotation direction corresponds to the rotation sense of the nuclear precession. This component of field can thus couple energy to the NMR process. The rotating field which derives from $B_{1x}\mathbf{a}_x$ and leads to nuclear resonance is therefore given by

$$\mathbf{B}_x^+ = (b_{xx} + ib_{yx})B_{1x}\mathbf{a}^+.$$ [8]

Similarly, the rotating field which results from linear excitation $B_{1y}\mathbf{a}_y$ is

$$\mathbf{B}_y^+ = (b_{xy} + ib_{yy})B_{1y}\mathbf{a}^+,$$ [9]

where

$$b_{xy} = b_{yx} \quad \text{and} \quad b_{yy} = -\psi_1\cos 2\phi + \psi_0.$$ [10]

Thus in the general case of elliptically polarized excitation $\mathbf{B}_1 = B_{1x}\mathbf{a}_x + iB_{1y}\mathbf{a}_y$, the rotating field components inside the cylinder are given by

$$\mathbf{B}^\pm = B^\pm\mathbf{a}^\pm,$$

where

$$B^+ = 1/2(b_{xx} + ib_{yx})B_{1x} + i/2(b_{xy} + ib_{yy})B_{1y},$$

$$B^- = 1/2(b_{xx}^* - ib_{yx}^*)B_{1x} + i/2(b_{xy}^* - ib_{yy}^*)B_{1y}. \qquad [11]$$

The extension to include the counter-rotating component (B^-) in Eq. [11] is straight-forward. For linear excitation B_{1x} or $B_{1y} = 0$, while for circular polarization $B_{1x} = B_{1y} = B_1$.

The magnetic field distribution for NMR excitation is given (with our convention) by B^+. Let us now calculate the NMR response to this excitation.

NMR response. Suppose that the density of spins within the cylinder is uniform. Then, the NRM response at each point depends only on the local field intensity and the pulse sequence. For simplicity we shall ignore relaxation effects, and for definiteness a spin-echo sequence is assumed. We consider, therefore, the spin-echo amplitude which results from the sequence $\theta_x-\tau-(2\theta)_y-\tau-$acq, where θ_α represents a spin nutation in the rotating frame through angle θ about an axis denoted by the subscript, and the echo time is 2τ. The spin nutation angle depends on the local field intensity and is therefore directly proportional to B^+. It is shown in the Appendix that the spin-echo response is given by

$$S_{SE} = S_0 \sin^3\theta(r, \phi), \qquad [12]$$

where S_0 depends on spin density (assumed uniform), and

$$\theta(r, \phi) = (\pi/2)B^+(r, \phi)/B_m^+, \qquad [13]$$

where the constant B_m^+ is the value of rf field necessary to produce a $\pi/2$ nutation angle (e.g., for a rectangular pulse with temporal width T, $B_m^+ = \pi/(2\alpha T)$, where α is the gyromagnetic ratio). Note that the spatial inhomogeneity of the NMR response thus derives from local variations in field intensity, and is a strong function of the spin flip angle set by the field.

Receiver response. The rf magnetic field which is set up by the precessing magnetization in response to the local excitation rotates at the Larmor frequency in the direction of the static precession. However, the voltage induced in the receiving coil has the opposite phase (8), and therefore the reception sensitivity distribution $R(r, \phi)$ is given by a function similar to B^-. Accordingly, let

$$R(r, \phi) = 1/2(b_{xx}^* - ib_{yx}^*)R_{1x} + i/2(b_{xy}^* - ib_{yy}^*)R_{1y}, \qquad [14]$$

where R_{1x} and R_{1y} are constants which describe the receiver polarization.

Total response. The expected image intensity at each point is given by a product of the transmission and reception distributions:

$$S(r, \phi) = S_{SE}(r, \phi)R(r, \phi). \qquad [15]$$

From [12] one obtains

$$S(r, \phi) = R(r, \phi)\sin^3[\varsigma B^+(r, \phi)], \qquad [16]$$

where ς is a constant.

Simulation Results

The program which evaluates Eq. [16] was formulated such that arbitrary degrees of ellipticity could be specified separately for the transmission and reception functions through choice of $B_{1\alpha}$ and $R_{1\alpha}$. We consider first linearly polarized transmission and reception (to model the usual single-port coil) and then present various combinations of rotating and linear polarizations.

Linear polarization. For the linear case both transmission and reception sensitivities are polarized along the x axis. Figure 3 shows results as the resistivity is varied while other parameters are kept fixed. The permittivity was chosen to approximate that of water at 64 MHz. At high resistivity the pattern is symmetric about the x axis since in this case the predominant current component is due to dielectric displacement. As the resistivity is decreased, a characteristic "quadrupole" artifact consisting of four "holes" is observed. These "holes" are caused by eddy currents which are inherently asymmetric and derive from the finite conductivity of the medium. Figure 4 shows simulations in which the relative permittivity is varied while other parameters are kept constant. As the permittivity is increased the wavelength within the cylinder decreases in accord with Eq. [6], and thus the electrical size of the cylinder (measured in wavelengths) becomes larger. The hole pattern therefore becomes more compressed

FIG. 3. Simulations of rf inhomogeneity for linear polarization as resistivity is varied. In lossless case pattern is symmetric about field. At lower resistivity, eddy currents cause quadrupole artifacts.
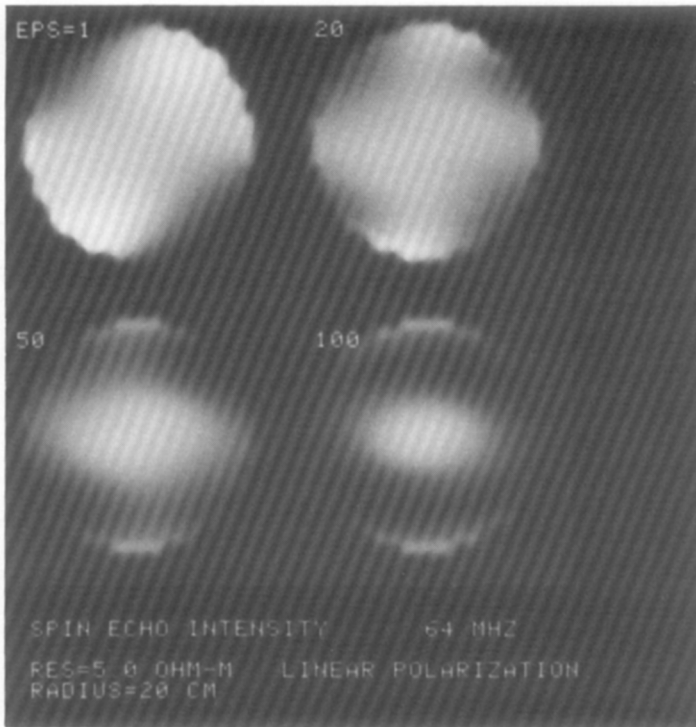
FIG. 4. Simulations of linear polarization with variable permittivity EPS. Increased EPS causes shorter wavelength in cylinder and concomitant shrinkage of artifact pattern.

in radial extent as the permittivity increases. Figure 5 shows simulations in which the cylinder diameter and frequency are varied. It may be seen that the artifacts are most predominant at highest frequency and largest diameter, for the same reasons given above.

Other polarization geometries. Figure 6 shows simulation results where the polarizations of transmit and receive fields are altered while other parameters are held constant. Comparison of Figs. 6A and B, wherein only the orientation of the receiver direction is altered, shows that two of the four "hole" artifacts result from the transmitter function ($S_E(r, \phi)$), and the other two derive from the receiver distribution ($R(r, \phi)$). This is further confirmed in Fig. 6C where rotating polarization is utilized in reception (which of course has no preferred orientation). Figures 6D and E show simulations with rotating polarization during transmission. When rotating reception is also used (Fig. 6E) the pattern becomes symmetric as expected since Cartesian axes are irrelevant. Comparison of Fig. 6E with Fig. 6A shows that the use of circular polarization for both transmission and reception can provide significant reduction of artifacts.

These simulations indicate that both conduction and displacement currents can be important in scanning torso sections. The artifact patterns depend on the size of the object relative to the wavelength. At 64 MHz, the half wavelength in a dielectric
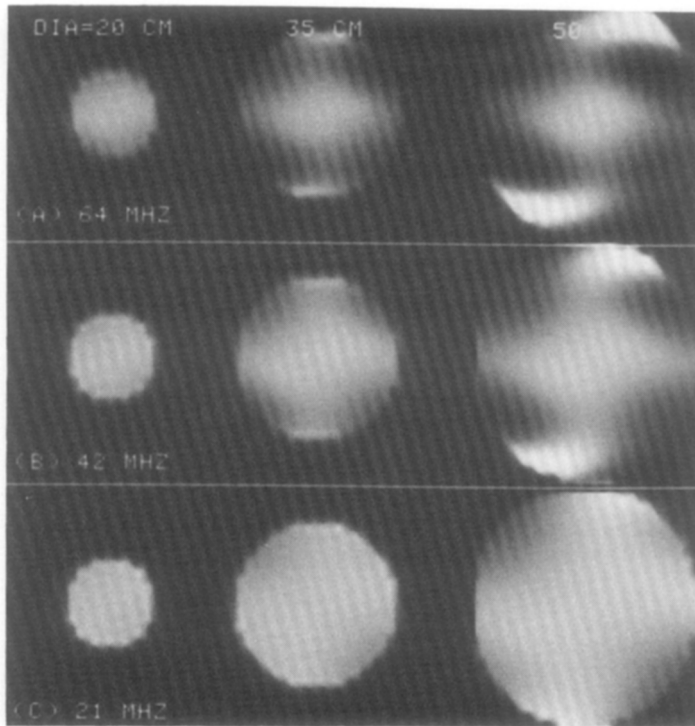
FIG. 5. Simulations with linear polarization as cylinder diameter and frequency are varied as shown. The relative permittivity and resistivity are 58 and 3.3 MΩ, respectively, for all images.

medium with $\epsilon_r = 100$ is about 25 cm, which is comparable to the size of typical human subjects. Thus the dielectric standing wave effects, modified by eddy currents, can produce substantial rf field nonuniformities.

Past discussions of rf inhomogeneity effects (*4, 6*) have described them in terms of field "penetration" limitations. In fact, one finds that for biological objects in the tens of megahertz range the rf field inside the subject is usually *larger* in magnitude than the external field because of standing wave effects. This occurs because the displacement current is larger or comparable to the conduction current. As the resistivity is decreased the conduction component eventually dominates and the field is then excluded from the object interior.

These results provided impetus for the comparative experimental investigation described in the next section.

EXPERIMENTAL INVESTIGATION

From the discussion of the preceding section, circular polarization can be excited in the object by two spatially orthogonal linear waves which are in time quadrature. Thus an rf coil having two independent, orthogonal modes is required in addition to appropriate means to drive the two ports in quadrature. The NMR signal presented
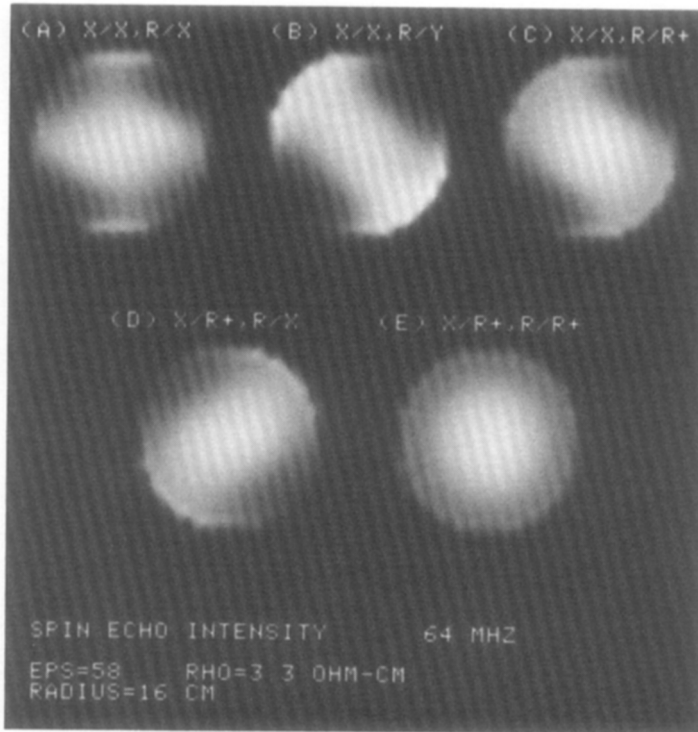
FIG. 6. Simulations with various combinations of transmitter (X/) and receiver (R/) polarizations (e.g., (D) is transmit with (+) rotating polarization, receive with linear polarization alone the x axis).

at the two ports must be combined with the opposite phase quadrature sense in order to receive with circular polarization.

Techniques

A flexible rf system was constructed for a 1.5 T imaging device as shown in Fig. 7. A two-port, 55 cm diam coil was arranged with the orthogonal axes at 45° to the x and y axis of the magnet. The two ports (labeled L and R for later reference in the images) had 28 dB isolation at the operating frequency as measured with a cylindrical, doped water phantom. Separate receiver and transmitter channels were provided for each port with computer controlled phase shifters and attenuators in one of the channels. In this fashion the ellipticity of receiver and transmitter polarizations could be independently controlled to any desired value including linear and circular (by controlling values analogous to B_{1x}, B_{1y}, R_{1x}, R_{1y} in Eqs. [11] and [14]).

The rf coil uses lumped element delay lines to produce two orthogonal, azimuthally sinusoidal current distributions (*10*). The coil is called a "birdcage" design because of the multiplicity of current-carrying conductors which generate the fields.

A cylindrical phantom (32 cm diam by about 40 cm long) was nearly filled with distilled water doped with $CuSO_4$ (to reduce T_1) and NaCl (to provide ionic conduc-
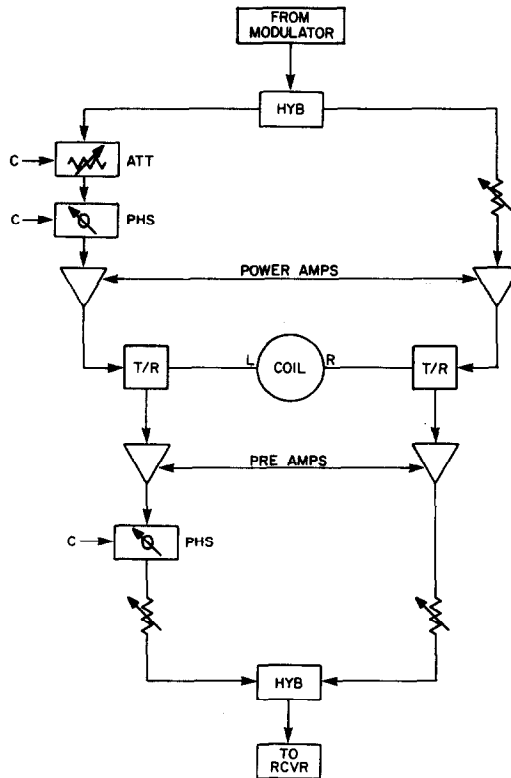
FIG. 7. Block diagram of experimental rf system for 1.5 T MR scanner. Phase shifter/attenuators allow arbitrary polarization of transmitter (XMTR) and receiver (RCVR) channels. HYB, hybrid network; T/R, transmit/receive switch; C, computer control; ATT, attenuator; PHS, phase shifter.

tivity) such that the relative permittivity was 58 and the resistivity was 3.3 Ω-m. These values provided an rf load to the coil which approximated that of a 50 kg person.

The degree of ellipticity was monitored in two ways. The first method used a probe constructed with two small, equidiameter search coils arranged coaxially with their planes parallel to the z axis. The coil polarities were chosen to oppose each other and their outputs were subtracted with a 180° hybrid network. In this way some immunity from common-mode, electric field-induced pickup was achieved. The detected probe output was monitored as a function of probe angle about the z axis while the transmitter phase shifter and attenuator were adjusted. Circular polarization was presumed when no amplitude variation with angle was observed.

The second method is based upon observation of the NMR signal from the object being scanned. The transmitters' relative phase and amplitude are adjusted for a null in the NMR signal, which corresponds to a circularly polarized wave rotating in the wrong sense. Once this null has been achieved, the correctly polarized condition is obtained by shifting the transmitters' relative phase by 180°. This method is far more convenient and accurate than the probe, and of course is performed with the subject

to be scanned in the coil. Nulls in excess of 40 dB were achieved with the water phantom described above. It was verified that a phase shift of 180° relative to the null indeed resulted in a maximum response as expected. After the transmitter was adjusted, the receiver polarization was tuned by the same null technique.

Phantom Results

Figures 8 and 9 show experimental results obtained with various combinations of linear and circular polarization similar to cases modeled in Fig. 6. The detailed qualitative agreement between the experimental and theoretical results provides confidence in the model. Note the nearly perfect null image obtained with the counter-rotating circular polarization direction (Fig. 9D). Other experiments were performed with undoped water phantoms and phantoms with smaller diameters. The results (not shown here) were in good agreement with the simulations (Figs. 3 and 4) and confirm the role of eddy currents in producing the asymmetric artifacts. Still other experiments used phantoms designed to minimize eddy currents. In one series, as a simple example, the cylindrical doped-water phantom was scanned as a function of slice position relative to the end of the phantom. As expected, when the slice was near the end the eddy currents were reduced and the images resembled the low-conductivity simulations
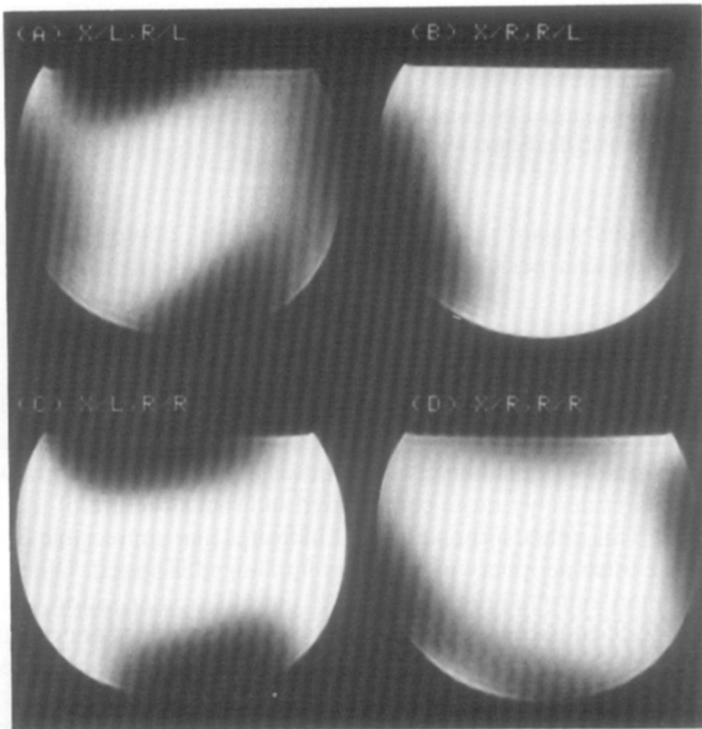

FIG. 8. Experimental scans of lossy water phantom at 1.5 T for linearly polarized transmitter and receiver (e.g., (C) is transmit left port, receive right port). (A) The usual single port, linear polarization case.
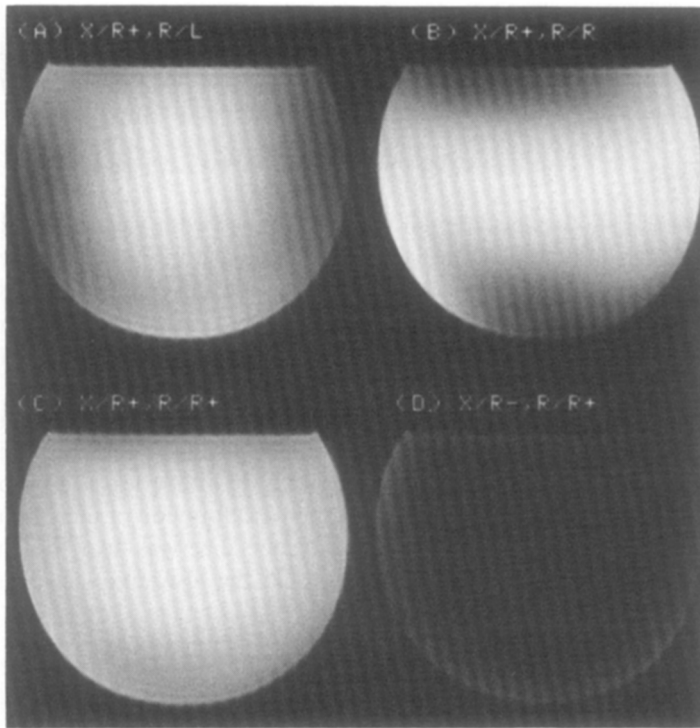
FIG. 9. Scans of lossy phantom with rotating excitation. Full rotating polarization (C) yields least artifacts; counter-rotating excitation (D) produces nearly null image.

(Fig. 3). These results suggest that the phantom geometry approximates the infinite-extent model if the scan position is greater than a skin depth from the end of the phantom.

Human Scans

A series of volunteers whose weights spanned 60 to 98 kg was scanned. A typical series is shown in Figs. 10 and 11. Note that the quadrupole artifact behavior observed with linear polarization is qualitatively the same as that with the uniform water phantom despite the considerably more complicated internal structure of the human abdominal section. This rather surprising result indicates that appreciable eddy currents can flow near the torso periphery where the rf flux linked is largest. Other similarities between the human and phantom scans using the other polarization configurations are observed as well. In particular, note that the "hole" artifacts are essentially eliminated when circularly polarized transmission and reception are employed and that the image obtained with counter polarized circular drive is an excellent null. Such nulls were routinely obtained with other subjects as well. This last result indicates that a high degree of circular polarization can be realized even in the practical case where the subject is highly nonuniform and not circularly symmetric. The good qualitative
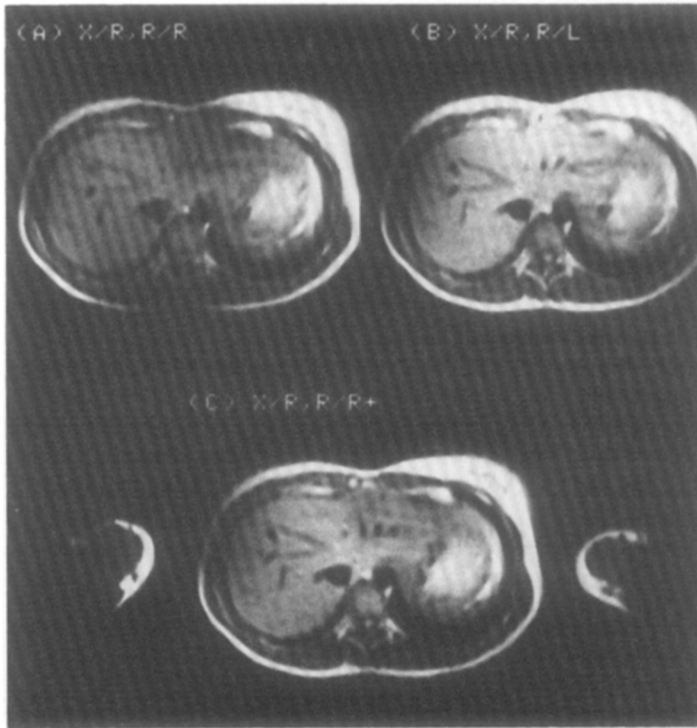
FIG. 10. Scans of human volunteers with linear excitation and (A) receive right port, (B) receive left port, (C) receive both ports (rotating polarization).

agreement between these results and the simulations again provides justification for the simple model.

Comparison of Radiofrequency Power and Signal-to-Noise Ratio

The peak power for the 700 μs π pulse was monitored. Typical results for rotating and linear excitation are shown in Table 1. The reported power for circular polarization is the sum of the powers in the two ports. Note that P_{rot}/P_{lin} factors of about 0.5 to 0.7 were observed. A factor of exactly 0.5 would be expected under ideal conditions with a symmetric geometry. Departures from that figure result for elliptic objects and imperfect rf components. (It is known, for example, that the rf power amplifiers were nonlinear at the higher power levels needed for linear excitation.) These imperfections were not compensated for in Table 1, however.

Figure 12 shows the measured and calculated relative rf power required to maximize the spin-echo response as a function of the phase angle between the coil excitation ports for a cylindrical phantom. At a differential phase of 90°, a purely rotating wave of the correct sense is achieved and the required drive power is minimized. At other phase angles, some of the applied power is dissipated in the counter-rotating mode and thus the applied power is higher. In particular, at 0° and at 180°, linear polarization is obtained and the required power is theoretically doubled.
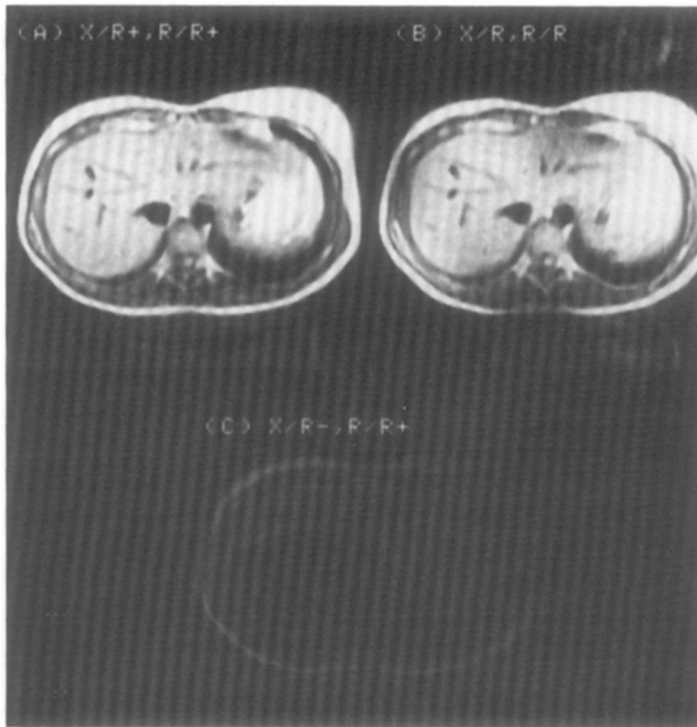
FIG. 11. (A, C) Scans of human volunteer with rotating excitation. Full circular polarization (A) greatly diminishes the quadrupole artifact with linear polarization (B).

The signal-to-noise ratio (SNR) was measured in reconstructed images of the cylindrical water phantom with linear and rotating reception. Rotating excitation was employed, and care was taken to remove low spatial-frequency shading from the noise determination. The results are shown in Table 2. The expected improvement (8) of $\sqrt{2}$ was obtained, and in fact a spuriously large factor was noted for circular polarization relative to the right channel despite care in matching the coil, preamp noise figures, and the other rf combiner network components. Similar data were obtained for human scans. In the comparison between linear and rotating polarization in Figs. 11A and B, the measured SNR improvement factor was 1.33. This figure was typical of human

TABLE 1

Radiofrequency Power Comparison

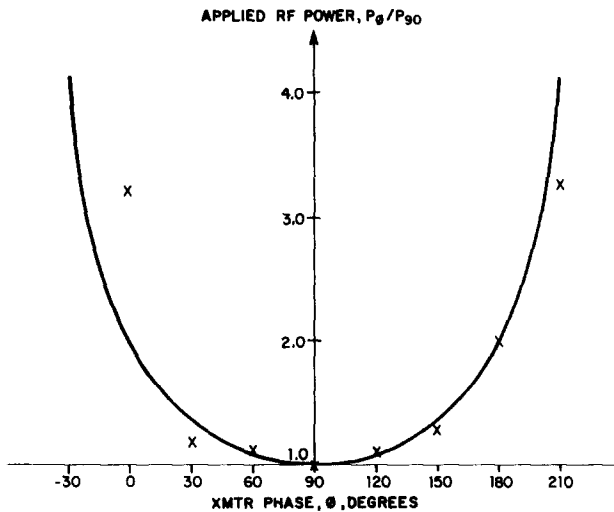| Subject	Weight (kg)	P_{rot} (kW)	F_{lin} (kW)	P_{rot}/P_{lin}
Phantom	—	1.9	3.2	0.59
"C"	59	4.4	6.2	0.71
"K"	82	4.7	10.1	0.47

FIG. 12. Calculated (solid) and measured relative rf drive power P required to maintain optimum spin-echo response for cylindrical water phantom as a function of relative phase ϕ between coil ports. 90° corresponds to circular polarization.

scans and reflects the asymmetric splitting of the body's thermal noise into the two orthogonal coil components.

SUMMARY

A simple model of rf inhomogeneity effects has been presented. The model has three components: calculation of the transmission distribution, NMR spin-echo response, and the receiver sensitivity distribution. The experimental results are in surprisingly good qualitative agreement with the simulations, considering the complexity of the body relative to the uniform cylinder model. This lends confidence in the use of such models to examine parametric behaviour of rf effects.

Artifacts are observed in objects which have dimensions comparable to a half wavelength. The artifacts are caused by dielectric standing wave effects and conduction (eddy) currents.

It was shown that use of circular polarization for both transmission and reception reduces the artifact intensity. Use of circular polarization for reception improves the

TABLE 2

S/N Comparison

Receiver configuration	S/N	Ratio rot/linear
Rotate	516	—
Linear/left	367	1.41
Linear/right	312	1.65

Run 05687.

signal-to-noise ratio by approximately the expected factor of $\sqrt{2}$. In addition, circularly polarized excitation reduces the rf drive power by a factor of 0.5 to 0.7 over linear drive, since the nonproductive counter-rotating mode is not excited. A factor of 0.5 would be expected for a symmetric object, while the smaller benefit is predicted for an object with elliptical cross section.

APPENDIX: SPIN-ECHO RESPONSE

Consider an isochromat undergoing the sequence $\theta_x-\tau-(2\theta)_y-\tau-$acq. Let $\Delta\omega$ be the offset frequency of the spin. If relaxation effects are ignored, the resulting magnetization during the acquisition period is

$$M_{acq} = R_z(\phi)R_y(2\theta)R_z(\phi)R(\theta)M_0, \qquad [A1]$$

where $R_\alpha(\theta)$ represents a rotation operator about axis α through angle θ, $M_0 = (0, 0, M_0)$ is the equilibrium magnetization, and $\phi = \Delta\omega\tau$. Evaluation of the matrices [7] yields

$$M_x(acq) = -\cos^2\theta \sin\theta \sin 2\phi + \sin 2\theta \cos\theta \cos\phi,$$

$$M_y(acq) = \sin\theta(\cos^2\phi - \cos 2\theta \sin^2\phi) + \sin 2\theta \cos\theta \sin\phi. \qquad [A2]$$

We now suppose there is an ensemble of isochromats with uniform distribution of offset frequencies (from T_2 and inhomogeneity broadening). Then the modulus of the total transverse signal M is

$$(2\pi|M|)^2 = \left\{\int_{-\pi}^{\pi} M_x d\phi\right\}^2 + \left\{\int_{-\pi}^{\pi} M_y d\phi\right\}^2. \qquad [A3]$$

The x component averages to zero, and the result is

$$M = M_0\sin^3\theta. \qquad [A4]$$

ACKNOWLEDGMENT

REFERENCES

1. D. I. HOULT AND P. C. LAUTERBUR, J. Magn. Reson. 34, 425 (1979).
2. P. A. BOTTOMLEY et al., Radiology 150, 441 (1984).
3. C-N. CHEN, V. J. SANK, AND D. I. HOULT, "Proceedings, Annual Meeting of the Society of Magnetic Resonance in Medicine, New York, New York, August 13–17, 1984," p. 148. (Abstract)
4. P. A. BOTTOMLEY AND E. R. ANDREW, Phys. Med. Biol. 23, 630 (1978).
5. P. MANSFIELD AND P. G. MORRIS, "Advances in Magnetic Resonance," Suppl. 2, "NMR Imaging in Biomedicine," p. 187, Academic Press, New York, 1982.
6. P. MANSFIELD AND P. G. MORRIS, "Advances in Magnetic Resonance," Suppl. 2, "NMR Imaging in Biomedicine," p. 182, Academic Press, New York, 1982.
7. E. T. JAYNES, Phys. Rev. 98, 1099 (1955).
8. C-N. CHEN, D. I. HOULT, AND V. J. SANK, J. Magn. Reson. 54, 324 (1983).
9. S. RAMO, J. R. WHINNERY, AND T. VANDUZER, "Fields and Waves in Communication Electronics," p. 329, Wiley, New York, 1965.
10. C. E. HAYES, W. A. EDELSTEIN, J. F. SCHENCK, O. M. MUELLER, AND M. EASH, J. Magn. Reson. 63, 622 (1985).